INTERNATIONAL JOURNAL FOR NUMERICAL METHODS IN FLUIDS
Int. J. Numer. Meth. Fluids 2009; **60**:972–991
Published online 16 October 2008 in Wiley InterScience (www.interscience.wiley.com). DOI: 10.1002/fld.1895

Jet impingement onto a tapered hole: Influence of jet velocity and hole wall velocities on heat transfer and skin friction

S. Z. Shuja, B. S. Yilbas*, † and S. M. A. Khan

ME Department, KFUPM, Dhahran 31261, Saudi Arabia

SUMMARY

Jet impingement onto a hole with elevated wall temperature can be associated with the high-temperature thermal drilling, where the gas jet is used for shielding the hole wall from the high-temperature oxidation reactions as observed in the case of laser drilling. In laser processing, the molten flow from the hole wall occurs; and in the model study, the hole wall velocity resembling the molten flow should be accounted for. In the present study, gas jet impingement onto tapered hole with elevated temperature is considered and the heat transfer rates as well as skin friction at the hole wall surface are predicted. The velocity of molten flow from the hole wall determined from the previous study is adopted in the simulations and the effect of hole wall velocity on the heat transfer rates and skin friction is also examined. It is found that the Nusselt number and skin friction at the hole wall in the regions of hole inlet and exit attain high values. The influence of hole wall velocity on the Nusselt number and skin friction is found not to be very significant. Copyright © 2008 John Wiley & Sons, Ltd.

Received 10 April 2008; Accepted 14 July 2008

KEY WORDS: jet; impingement; hole; Nusselt number; skin friction

1. INTRODUCTION

In laser gas-assisted processing, an impinging jet is used to shield the irradiated region from the oxidation reactions. In most cases, the jet emanates from a conical nozzle coaxially with the laser beam. The surface of the molten material in the irradiated region moves in the direction of gravity with the influence of the drag force generated by the assisting gas. Therefore, the heat transfer rates as well as the skin friction are influenced by the coupling effect of the impinging jet and the moving molten surface. This, in turn, alters the end-product quality. In this case, the moving molten surface generates a slip boundary for the impinging jet in the irradiate region. However,

*Correspondence to: B. S. Yilbas, ME Department, KFUPM, Dhahran 31261, Saudi Arabia.
†E-mail: bsyilbas@kfupm.edu.sa

Contract/grant sponsor: King Fahd University of Petroleum and Minerals, Dhahran, Saudi Arabia

the velocity of the molten surface depends on the laser output power such that it increases with increasing the laser output power, i.e. the velocity of the molten surface changes once the laser output power intensity is modified. Consequently, investigation into jet impingement onto the moving surface resembling laser processing, such as drilling, becomes necessary.

Considerable research studies have been carried out to examine jet impingement onto heated surfaces. The effects of nozzle inlet chamfering on the pressure drop and heat transfer in confined air jet impingement were studied by Brignoni and Garimella [1]. They indicated that the ratio of average heat transfer coefficient to pressure drop was enhanced by as much as 31% due to chamfering of the nozzle, showing that narrow chamfering resulted in improved performance. The effect of nozzle aspect ratio on stagnation region heat transfer characteristics of impinging jet was investigated by Jungho and Lee [2]. They showed that for small spacing between the nozzle to plate, the heat transfer rate increased larger for the elliptic jet than that of the axisymmetric jet in the stagnation region. Impinging jet cooling of concave surfaces was studied by Souris *et al.* [3]. They indicated that the approach adopted in the numerical solution provided low-cost and accurate predictions of heat transfer rates. The heat transfer between a uniformly heated plate and an impinging circular arc jet was investigated experimentally by Haung and El-Genk [4]. They showed that jet flow had a bell-shape nature and the Nusselt number increased as the jet size increased at the plate surface. A slot jet impingement due to cooling of concave surface and the effects of nozzle configuration were examined by Yang *et al.* [5]. They showed that the average heat transfer rates for impingement on the concave surface were more enhanced than that of the flat surface because of curvature effect. The local heat transfer characteristics of air jet impingement for nozzle–plate spacing less than one nozzle diameter were examined experimentally by Lytle and Webb [6]. They showed that the effects of an accelerating fluid in the nozzle–plate gap as well as transition from a laminar to a turbulent boundary layer resulted in a significant increase in the local heat transfer rates. The flow field due to an impinging jet emanating from a rectangular slot nozzle at high Reynolds number was examined by Cziesla *et al.* [7]. They used a large eddy simulation technique in the numerical computation and indicated that results compared favorably with the experimental results, particularly in the stagnation zone. The effects of nozzle diameter on heat transfer and fluid flow due to jet impingement on a flat plate were examined by Lee *et al.* [8]. They indicated that the local Nusselt number increased with increasing nozzle diameter in the stagnation region, which might be attributed to an increase in the jet momentum and turbulence intensity level with the large nozzle diameter. The effect of nozzle geometry on local convective heat transfer due to a confined impinging air jet was investigated by Colucci and Viskanta [9]. He showed that the local heat transfer coefficients for confined jets were more sensitive to Reynolds number and nozzle-to-plate spacing than those for unconfined jets. Turbulent axisymmetric jets impinging on a flat plate and flowing into an axisymmetric cavity were studied by Amano and Brandt [10]. They indicated that a k–ε turbulence model resulted in good predictions of the velocity, pressure, and skin friction distributions. Shuja *et al.* [11, 12] investigated jet impingement onto a flat plate as well as onto the cavities. They also showed that the heat transfer rates and skin friction were affected by the cavity size and the nozzle cone angle.

In laser drilling process, the size of the hole can be few millimeters to tens of micrometers depending on the requirements. In cooling applications, in general, millimeter size holes are favorable to be drilled in the substrate material. The heat transfer rates and the flow structure developed inside hole influence the end-product quality. However, the measurement of the heat transfer rates and the flow structures within the hole is difficult due to the high temperature of the hole wall and the small hole diameter. Therefore, the model study offers predictions of heat transfer

DOI: 10.1002/fld

rates and skin friction at the wall surface, which are useful for understanding of the physical processes taking place during laser gas assisted drilling. Although jet impingement onto a hole at elevated wall temperature, resembling the laser drilling was investigated before [13], the hole wall was assumed to be stationary in the simulations. However, in the actual situation, the liquid layer developed around the hole wall moves downwards under the influence of the gravity and the drag force developed by the assisting gas. Consequently, when modeling such a flow situation, the movement of the hole wall needs to be considered in the analysis. In the present study, jet impingement onto a tapered hole with elevated wall temperature in relation to laser drilling is considered and the effect of jet and wall velocities on the heat transfer rates and skin friction was examined. In the simulations, six wall velocities and two jet velocities are accommodated while air is considered as working fluid.

2. MATHEMATICAL MODELING

The mathematical analysis presented below is similar to an earlier work [12]. However, for completeness of the analysis, the arrangements of equations and some details of the turbulence model as well as boundary conditions are given. The geometric arrangement of the nozzle and the tapered hole is shown in Figure 1, while the nozzle and the hole configurations are listed in Table I. It should be noted that the dimensions used in the simulations are similar to those used in the actual situations.

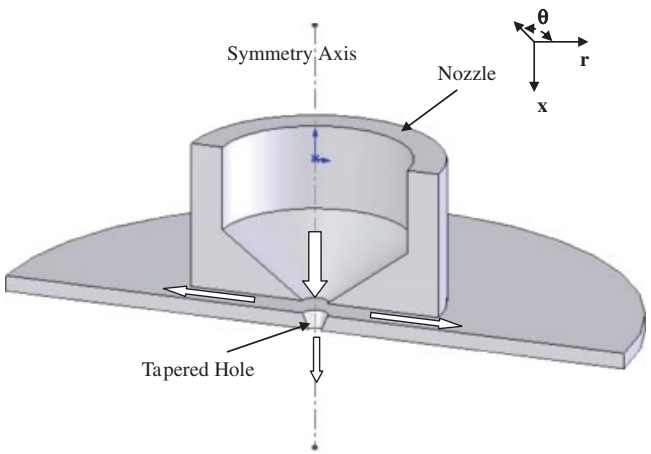

Figure 1. Schematic view of the nozzle and the tapered hole. Arrows show the flow directions.

Table I. Diameter and depth of the hole, and nozzle exit diameter.

Hole diameter (m)	Hole thickness (depth) (m)	Hole taper angle (deg.)	Nozzle exit diameter (m)
0.001	0.002	45	0.0004

DOI: 10.1002/fld

The steady and axisymmetric flow conditions are considered and the compressibility and variable properties of the working fluid are accommodated in the analysis. A constant temperature is considered at the hole wall to resemble the laser produced hole, i.e. the hole wall temperature is kept at 1500 K as similar to the melting temperature of the substrate material. In addition, the hole wall is assumed to move with a velocity similar to the molten metal velocity as determined from the previous study [14]. Consequently, six hole wall velocities are considered in the simulations to cover the large variation of hole wall velocities. These are 0, 5, 10, 20, 25, and 30 m/s.

2.1. Flow equations

The governing flow and energy equations for the axisymmetric impinging steady jet can be written in the Cartesian tensor notation as:

(i) The continuity equation

$$\frac{\partial}{\partial x_i}(\rho U_i)=0 \tag{1}$$

(ii) The momentum equation

$$\frac{\partial}{\partial x_i}(\rho U_i U_j)=\frac{\partial p}{\partial x_j}+\frac{\partial}{\partial x_i}\left[\mu\left(\frac{\partial U_i}{\partial x_j}+\frac{\partial U_j}{\partial x_i}\right)-\rho R_{ij}\right] \tag{2}$$

(iii) The energy equation

$$\frac{\partial}{\partial x_i}(\rho U_i H)=\frac{\partial}{\partial x_i}\left[\frac{\mu}{\sigma}\frac{\partial H}{\partial x_i}-\rho R_{ih}\right] \tag{3}$$

The flow field is turbulent; therefore, Reynolds stress turbulence model (RSM), which is based on the second-moment closure, is used in the analysis. The transport equation of the Reynolds stress (R_{ij}) is

$$\frac{\partial}{\partial x_m}(U_m R_{ij})=P_{ij}+\Lambda_{ij}-\varepsilon_{ij}+\Pi_{ij}+\Pi_{ij}^{\mathrm{w}} \tag{4}$$

where P, Λ, ε, Π, and Π^{w} are the rate of production, transport by diffusion, rate of dissipation, transport due to turbulent pressure excluding strain interactions, and transport due to wall reflection, respectively. Equation (4) consists of six partial differential equations; one for the transport of each of the six independent Reynolds stresses. The production term (P_{ij}), diffusion (Λ_{ij}), dissipation (ε_{ij}), transport due to turbulent pressure (Π_{ij}), and the modeling of the wall reflection (Π_{ij}^{w}) are defined as in [15].

2.2. Flow boundary conditions

Four boundary conditions are considered in accordance with the geometric arrangement of the problem, as shown in Figure 2.

DOI: 10.1002/fld

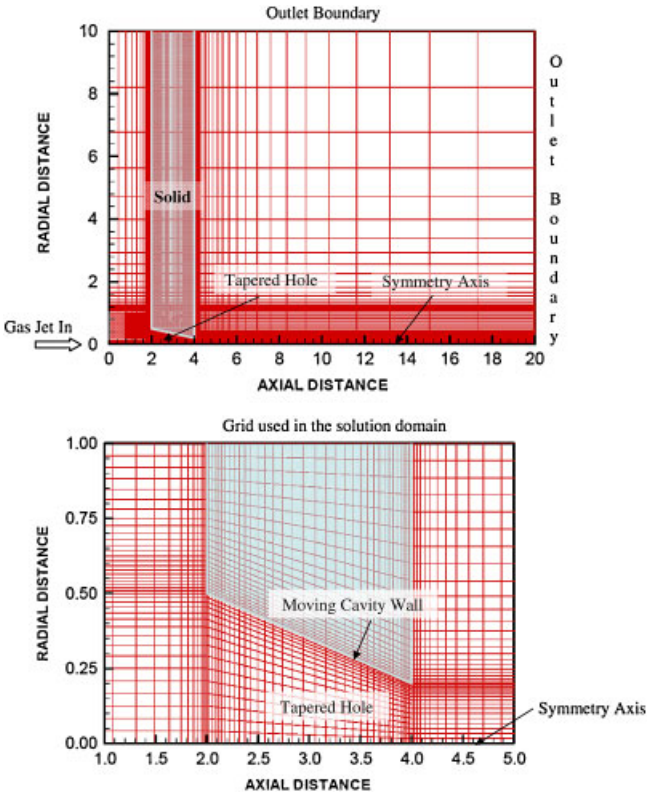

Figure 2. Solution domain and grid used in the simulations.

2.2.1. Solid wall. For the solid wall, the slip condition is assumed (except $U_{\text{wall}} = 0\,\text{m/s}$) according with the hole velocity resembling the molten flow [14], and the boundary condition for the velocity at the solid wall therefore is

$$U_i = U_{\text{wall}} \tag{5}$$

2.2.2. Generalized wall functions for normal and shear turbulent stresses for the RSM model. When the flow is very near the wall, it undergoes a rapid change in direction; therefore, the wall-functions approach is not successful in reproducing the details of the flow. Consequently, the turbulent stresses and fluxes at the near-wall grid points are calculated directly from their transport equations. In this case, the near-wall region lying between the wall and the near-wall computational node at x_{p} can be represented by two layers: the fully viscous sublayer, defined by $Re_{\text{v}} = x_{\text{v}}\sqrt{k_{\text{v}}}/v \approx 20$ and a fully turbulent layer. The wall shear stress near the wall is employed, i.e. $\overline{vw}|_{z_{\text{v}}} = \tau_{\text{w}}/\rho$, which serves as the boundary condition for the $\overline{vw}$ transport equation.

In relation to normal stresses, the turbulence energy must decrease quadratically toward a value of zero at the wall; therefore, a zero-gradient condition for the normal stresses is physically realistic. This is because of the viscous shear layer; in which the turbulence shear stress is zero within this layer. In addition, this situation is insufficient to ensure an accurate numerical representation of

DOI: 10.1002/fld

near-wall effects. An improved approach for internal cells is needed with respect to evaluating volume-integrated production and dissipation of normal stresses (these are normally evaluated at cell centers, using linear interpolation, and then multiplied by the cell volume). Considering $\overline{v^2}$ as an example, the volume-integrated production of $\overline{v^2}$ between the wall and the P-node may be approximated by [16]

$$\int_{\Delta r}\int_0^{z_\mathrm{p}} P_{22}\,\mathrm{d}\forall \cong \int_{\Delta r}\int_{x_\mathrm{v}}^{x_\mathrm{p}} -2\overline{vw}\frac{\partial V}{\partial x}\,\mathrm{d}\forall = 2\tau_\mathrm{w}\left(\frac{V_\mathrm{p}-V_\mathrm{v}}{x_\mathrm{p}-x_\mathrm{v}}\right)x_\mathrm{p}\Delta r \tag{6}$$

where V_p and V_v follow from the log law. No contribution arises from the viscous sublayer, since $\overline{vw}=0$ in this layer. An analogous integration of the dissipation rate with the assumptions

$$\varepsilon = \frac{2\nu k_\mathrm{v}}{x_\mathrm{v}^2}, \quad 0 \leqslant x \leqslant x_\mathrm{v}$$

$$\varepsilon = \frac{C_\mu^{3/4} k_\mathrm{p}^{3/2}}{\kappa x_\mathrm{v}}, \quad x_\mathrm{v} \leqslant x \leqslant x_\mathrm{p}$$

leads to

$$\int_{\Delta r}\int_0^{x_\mathrm{p}} \varepsilon\,\mathrm{d}\forall \cong \left[\frac{2\nu k_\mathrm{p}}{x_\mathrm{v}} + \frac{C_\mu^{3/4} k_\mathrm{p}^{3/2}}{\kappa}\ln\left(\frac{x_\mathrm{p}}{x_\mathrm{v}}\right)\right]\Delta r \tag{7}$$

and an analogous treatment is applied to $\overline{v^2}$, while the production of $\overline{w^2}$ in the viscous and turbulent near-wall layers region is zero.

The values resulting from Equations (6) and (7) are added, respectively, to the volume-integrated generation and dissipation computed for the upper half of the near-wall volume. It should be noted that for the wall-law approach, the near-wall dissipation (ε_p) is not determined from its differential equation applied to the near-wall cell surrounding the node. Instead, and in accordance with the log law, this value is obtained via the length scale from $\varepsilon_\mathrm{p} = C_\mu^{3/4} k_\mathrm{p}^{3/2}/\kappa z_\mathrm{p}$, which serves as the boundary conditions for inner cells.

2.3. Inlet conditions

The boundary conditions for temperature (T = specified, 300 K) and the mass flow rate at the nozzle exit are introduced. The mass flow rate at the nozzle exit is changed for each case considered such that the mean jet velocities at the nozzle exit are 50 and 100 m/s. The selection of the average velocities at the nozzle exit is based on the actual laser cutting situations [14].

The values of κ and ε are not known at the inlet, but can be determined from the turbulent kinetic energy, i.e.

$$k = \lambda \bar{u}^2 \tag{8}$$

where $\bar{u}$ is the average inlet velocity and λ is a percentage.

The dissipation is calculated from $\varepsilon = C_\mu k^{3/2}/aD$, where D is the diameter. The values $\lambda = 0.03$ and $a = 0.005$ are commonly used and may vary slightly in the literature [17].

DOI: 10.1002/fld

2.4. Outlet

The flow is considered to be extended over a long domain; therefore, the boundary condition (outflow boundaries) for any variable ϕ is

$$\frac{\partial \phi}{\partial x_i} = 0 \tag{9}$$

where x_i is the normal direction at outlet.

2.5. Symmetry axis

At the symmetry axis, the radial derivative of the variables is set to zero, i.e.

$$\frac{\partial \phi}{\partial r} = 0 \tag{10}$$

except for

$$V = \overline{vw} = \overline{vh} = \overline{wh} = 0 \tag{11}$$

2.6. Solid side

2.6.1. Constant wall temperature boundary. Two constant temperature boundaries are considered. The first one is in the radial direction far away from the symmetry axis at a constant temperature $T = T_{\text{amb}}$ (300 K). It should be noted that the constant temperature boundary condition is set at different locations in the radial directions. The boundary condition ($T =$ constant) located in the radial direction had no significant effect on the temperature and flow field in the stagnation region. Therefore, this boundary condition is set for a radial distance of 0.0005 m from the symmetry axis. The second constant temperature boundary is set at the hole walls at $T =$ constant (1500 K).

2.6.2. Solid–fluid interface. The coupling of conduction within the solid and convection within the fluid is required for the present analysis. At the solid–fluid interface, the appropriate boundary condition is the continuity of heat flux, i.e.

$$K_{\text{w}_{\text{solid}}} \frac{\partial T_{\text{w}_{\text{solid}}}}{\partial x} = K_{\text{w}_{\text{gas}}} \frac{\partial T_{\text{w}_{\text{gas}}}}{\partial x} \tag{12}$$

At the hole wall, a constant temperature boundary is assumed. The assumption of the constant temperature boundary is due to the high hole temperature which resulted during the laser processing; in which case, the hole wall temperature remains almost at the melting temperature of the substrate material (for mild steel, $T_{\text{w}} \sim 1500$ K).

No radiation loss from the solid surface is assumed, which is because of the small hole size.

The heat transfer coefficient is defined from the Fourier heat law:

$$h_{\text{s}} = \frac{K_{\text{f}}(\partial T/\partial n)_{\text{wall}}}{(T_{\text{w}} - T_{\text{ref}})} \tag{13}$$

DOI: 10.1002/fld

where K_f is the fluid thermal conductivity, $(\partial T/\partial n)_{wall}$ is the temperature gradient within the neighborhood of the wall, T_w is the wall temperature, and T_{ref} is the reference temperature. In the present case $T_{ref} = T_j$.

2.6.3. Solid heating. In the solid, the conduction heat transfer is considered and the Fourier heating law is accommodated. Temperature is assumed to reduce the reference temperature at a distance far away from the hole wall. Consequently, the boundary condition for the solid is at a distance far way from the wall, $T = 300\,\text{K}$.

2.7. Working fluid and solid

Air is used as a working fluid and it is assumed to be an ideal gas; therefore, the equation of state and related equations is adopted for the property calculations. Steel is used as the solid substrate in the simulations. Table II gives the thermal properties of steel at 300 K.

3. NUMERICAL METHOD AND SIMULATION

A control volume approach is employed to discretize the governing equations. The discretization procedure is given in the literature [18]. The problem of determining the pressure and satisfying continuity may be overcome by adjusting the pressure field so as to satisfy continuity. A staggered grid arrangement is used in which the velocities are stored at a location midway between the grid

Table II. Thermal properties of steel at 300 K.

	Specific heat capacity (J/kg K)	Thermal conductivity (W/mK)	Density (kg/m^3)	Thermal diffusivity (m^2/s) $\times 10^{-6}$
Steel	502.48	150	8030	37.175

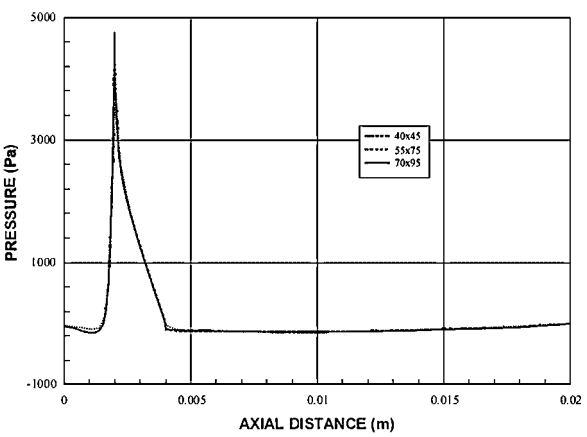

Figure 3. Grid independent test results. Pressure along the symmetry axis is shown for different grid sizes for the jet velocity of 100 m/s and the wall velocity of 30 m/s.

DOI: 10.1002/fld

points, i.e. on the control volume faces. All other variables including pressure are calculated at the grid points. This arrangement gives a convenient way of handling the pressure linkages through the continuity equation and is known as Semi-Implicit Method for Pressure-Linked Equations (SIMPLE) algorithm. The details of this algorithm are given in the literature [18].

The computer program used for the present simulation can handle a non-uniform grid spacing. In each direction, a fine grid spacing near the gas jet impingement point and the hole is allocated while gradually increased spacing for locations away from the hole is considered (Figure 2). Elsewhere the grid spacing is adjusted to maintain a constant ratio of any of the two adjacent spacing. The numbers of grid planes used normal to the ξ and ρ directions are 70 and 95 (70×95), respectively, in the simulations. The grid independence tests were conducted. The mesh resulting in grid independent solution is selected for the simulations (70×95 mesh size). The pressure variation along the symmetry axis for the jet velocity of 100 m/s and the wall velocity of 30 m/s is shown in Figure 3 for different grid sizes.

Nine variables are computed at all grid points, these are: two velocity components, local pressure, five turbulence quantities, and temperature.

4. RESULTS AND DISCUSSIONS

Flow impinging onto a conical hole with an elevated wall temperature is considered and the flow field in the region of the hole is predicted. The hole wall is assumed to have a velocity and is tapered to resemble the laser drilled hole situation. The velocity of the hole wall is varied in accordance with the findings of a previous study [14]. Heat transfer coefficient and skin friction at the hole wall are predicted for various impinging jet and hole wall velocities. The geometric length scales in the figures are non-dimensionalized through dividing the nozzle exit diameter.

Since there is no experimental and theoretical data in the open literature for the flow situation adopted in the present study; the experimental data for the jet impingement and heat transfer onto a flat plate are used for the model validation purpose [19]. The boundary and flow conditions are changed accordingly to simulate the experimental test conditions such that the Reynolds number at the nozzle exit is set at $Re = 23\,000$ and the flat plate boundary conditions are adopted [19]. It can be seen from Figure 4 that velocity distributions predicted along the axial distance (along the

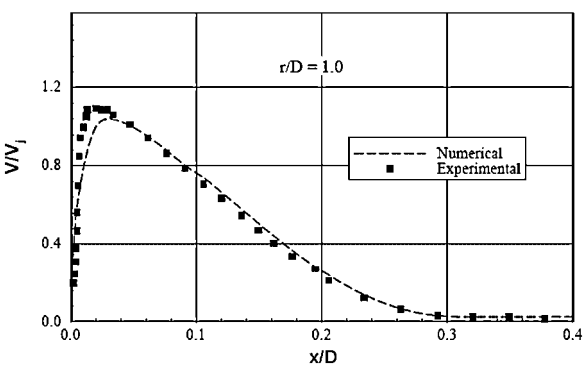

Figure 4. Normalized velocity magnitude along the axial distance at radial location of $r/D = 1$ obtained from predictions and the experiment [19].

DOI: 10.1002/fld

x-axis, normal to the hole inlet surface plane) at a radial location $r/D=1$ are in good agreement with the experimental data.

Figure 5 shows velocity vectors in the close region of the hole for two impinging jet and six hole wall velocities. In general, the jet bending and the streamline curvature are evident in the neighborhood of the hole inlet. This is because of the blockage effect of the hole; in which case, flow entering into the hole results in pressure increase in the region of the hole inlet because of the hole convergence (tapering). This is more pronounced in the region of the hole circumference. The streamline curvature above the hole inlet causes flow spilling in the region of the hole circumference. This situation is observed for all jet and wall velocities. Since the flow in the hole

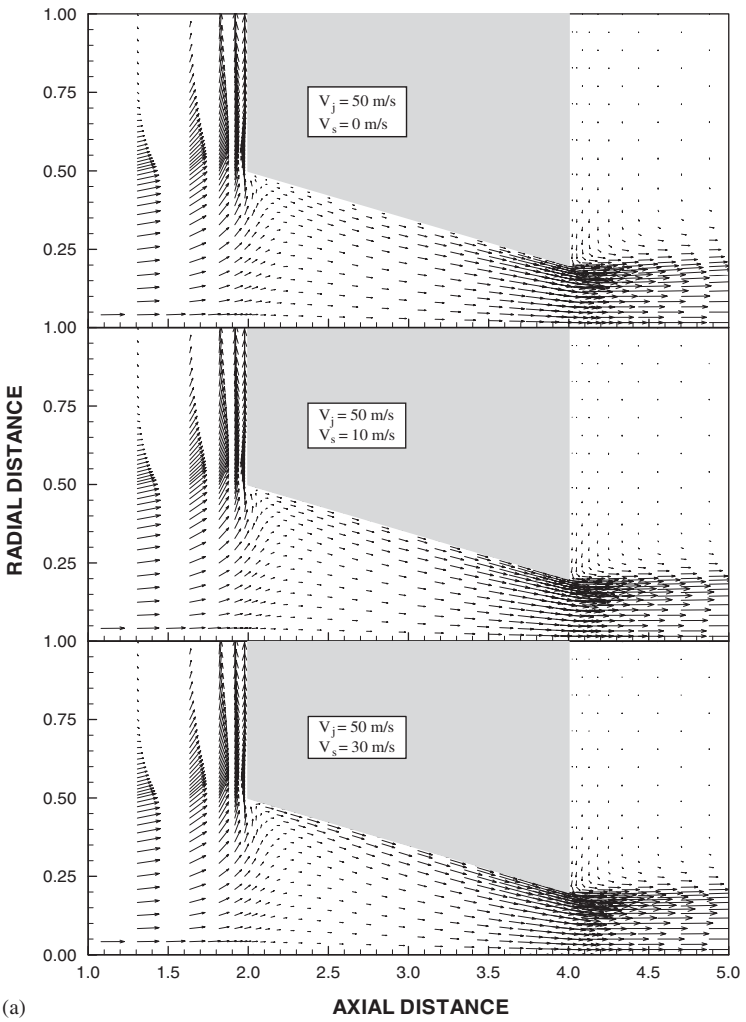

(a)

Figure 5. Normalized velocity vectors (V/V_j) around the hole. Mean jet velocity at nozzle exit is: (a) 50 m/s and (b) 100 m/s. The axial and radial distances are normalized by dividing the nozzle exit diameter (D). Taper angle is 45°.

DOI: 10.1002/fld

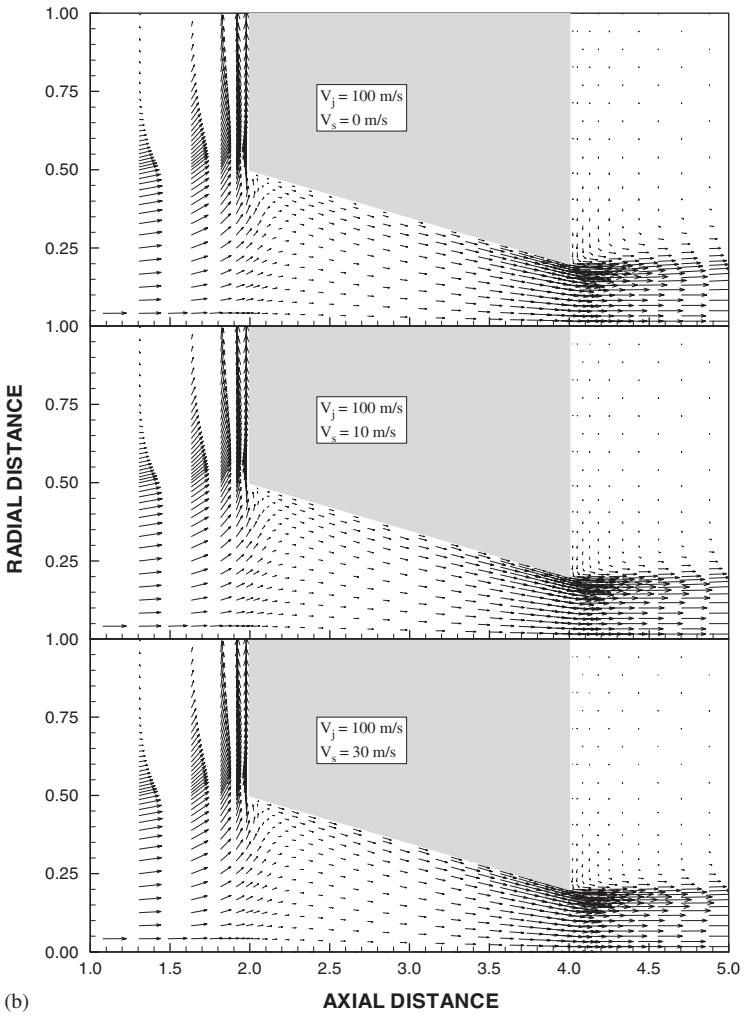

(b)

Figure 5. *Continued.*

is subsonic, hole convergence results in the acceleration of flow in the hole toward the hole exit. Consequently, flow forms a jet upon leaving the hole. This situation is more pronounced for the high jet velocity (100 m/s). Although the shear layer developed at the jet boundary is evident, no circulation is formed in the neighborhood of the jet boundary leaving the hole. The influence of the hole wall velocity on the flow structure is not significant because of the confined flow situation in the hole, which suppresses the radial expansion of the flow. However, at the hole inlet radial momentum toward the hole wall generates a radial flow in this region. This decays significantly as the flow progresses in the axial direction. The effect of jet velocity on the flow field in the hole is not significant, except close to the moving wall. This is more pronounced for high hole wall velocity (30 m/s); in which case, the axial momentum of the flow in this region increases the velocity magnitude in the near-wall region.

DOI: 10.1002/fld

Figure 6 shows dimensionless pressure contours for two jet and three hole wall velocities, respectively. Pressure increases in the jet above the hole because of the blockage effect. However, the region in which pressure builds up extends in the axial direction (toward the jet) and in the radial direction (next to the circumference of the hole). The extension of the region, in which pressure is built up, is because of the streamline curvature of the impinging jet, i.e. change of axial momentum into radial momentum is responsible for the extension of the high-pressure region. This situation is true for all velocities considered in the simulations; increasing pressure in the cavity is because of the blockage effect due to convergence of the cavity. In this case, flow impinging into the hole suffers from the blockage effect and the converging area of the nozzle cannot accommodate high velocity flow in the hole. Consequently, velocity decreases and pressure increases. However, toward the exit of the hole, because of converging hole wall flow accelerates and convective acceleration of the flow reduces the pressure in the exit region of the cavity. The

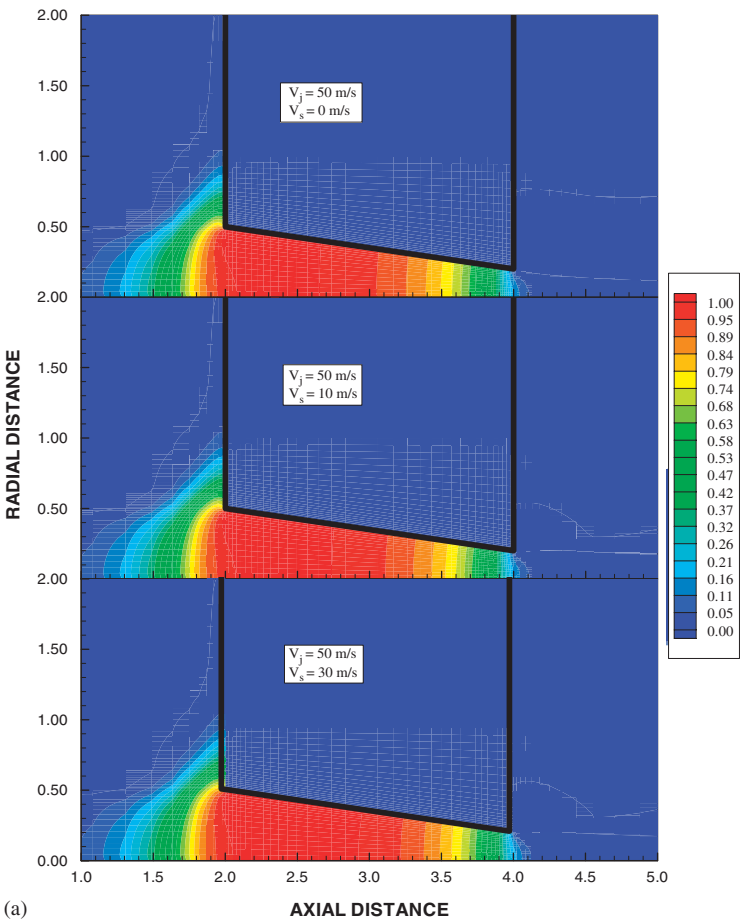

Figure 6. Pressure coefficient around the hole. Mean jet velocity at nozzle exit is: (a) 50 m/s and (b) 100 m/s. The axial and radial distances are normalized by dividing the nozzle exit diameter (D). Taper angle is 45°.

DOI: 10.1002/fld

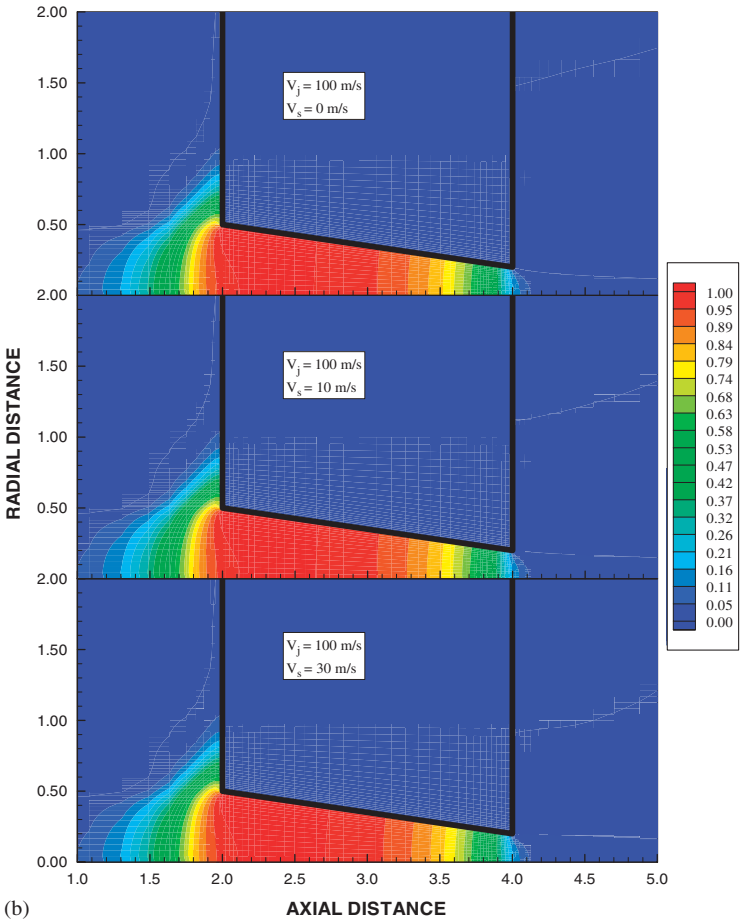

(b)

Figure 6. *Continued.*

influence of the hole wall velocity on the pressure field in the hole is not significant. This situation is true for all jet velocities.

Figure 7 shows temperature contours in the close region of the hole for two jet and three different wall velocities. Fluid temperature increases in the region of the hole walls due to convective and conduction heating of the fluid from the hole wall since the hole wall temperature is 1500 K. The stagnation point heating in the hole entry region contributes to fluid temperature enhancement. This extends in the radial direction toward the hole circumference because of the streamline curvature. The fluid heating in the region of the hole wall increases the static pressure because of the assumption of an ideal gas for the working fluid. Although the thermal boundary thickness is small, pressure increase in this region enhances the blockage effect in the hole. However, the hole wall velocity influences slightly the temperature of the jet at the hole exit. In this case, increasing the hole wall velocity increases the size of the high-temperature region in the jet exiting the hole. This is more pronounced for high wall velocity (30 m/s). Moreover, increasing the jet velocity suppresses the thickness of the thermal boundary layer in the region near to the hole wall, which

DOI: 10.1002/fld

in turn lowers the blockage effect in the hole, particularly at hole exit region. This enhances the flow acceleration at the exit of the hole.

Figure 8 shows the Nusselt number variation along the hole wall for two jet and six hole wall velocities. It should be noted that the dimensionless distance 0 represents the hole inlet while 2 represents the hole exit. The Nusselt number attains high values at the hole inlet and it decreases sharply with increasing distance along the wall from the hole inlet toward the hole exit. Attainment of the high Nusselt number is because of the fluid temperature at the hole inlet, which is low (300 K); consequently, temperature gradient between the fluid and the hole wall is high. This situation is true for all jet and hole wall velocities, despite the fact that at the hole inlet radial momentum of the flow due to streamline curvature is large while axial momentum is small. As the flow in the hole wall region progresses further toward the hole exit, fluid temperature rises while

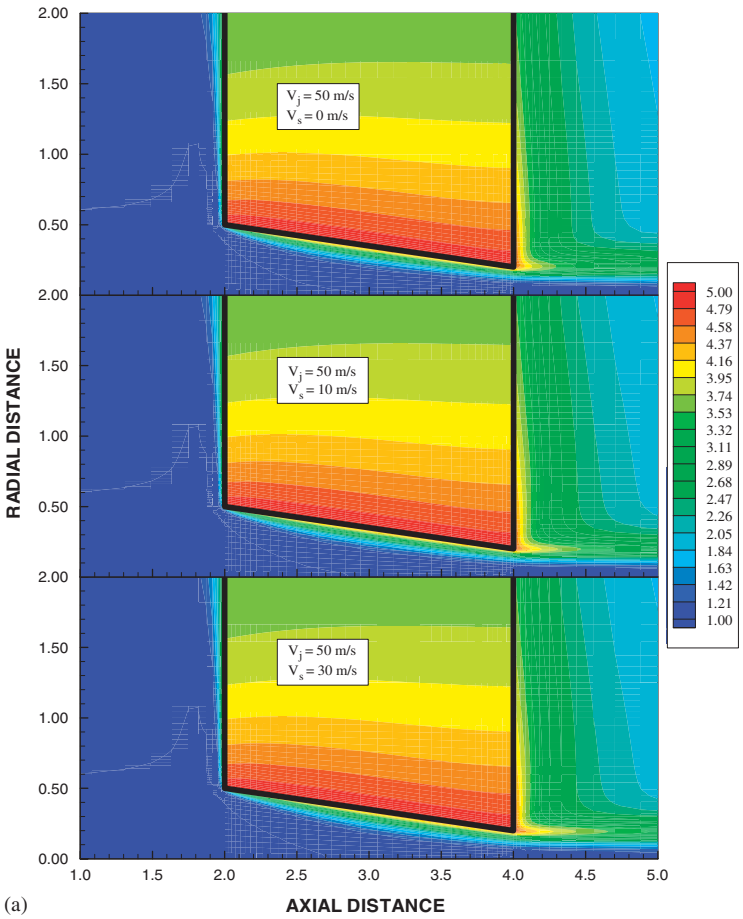

(a)

Figure 7. Normalized temperature (T/T_j) distribution around the hole. Mean jet velocity at nozzle exit is: (a) 50 m/s and (b) 100 m/s. The axial and radial distances are normalized by dividing the nozzle exit diameter (D). Taper angle is 45°.

DOI: 10.1002/fld

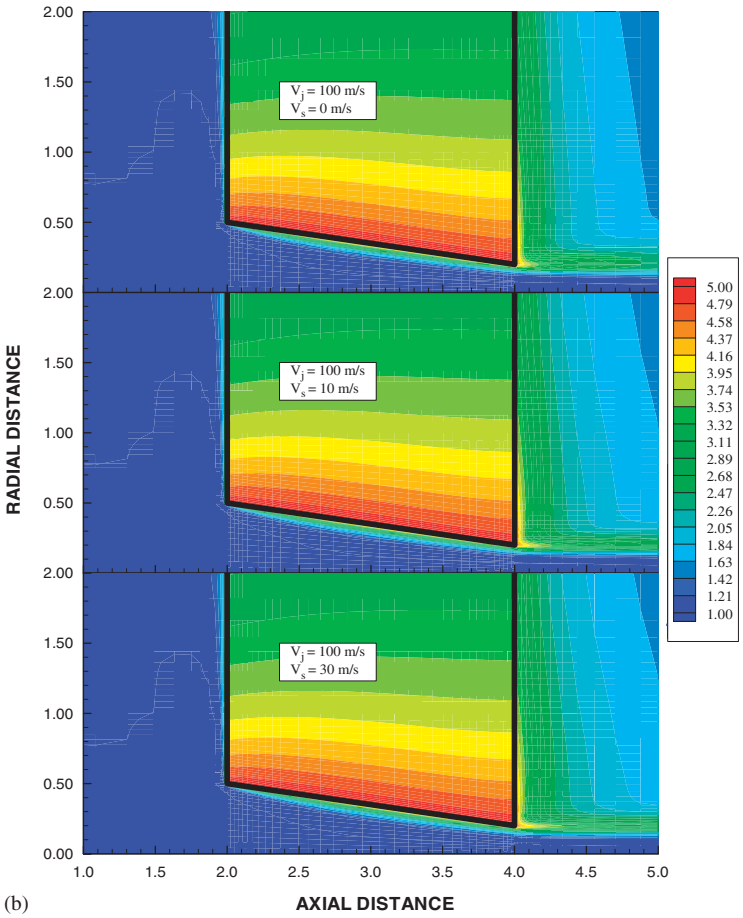

(b)

Figure 7. *Continued.*

lowering the temperature gradient in this region. The Nusselt number reduces as a consequence of this situation. In the case of hole exit, the flow acceleration enhances the Nusselt number slightly in this region despite the increased fluid temperature. This situation is true for all jet velocities. The influence of the hole wall velocity on the Nusselt number is not significant, provided that at the hole inlet, the Nusselt number increases slightly with increase in the hole wall velocity while the opposite is true in the region of the hole exit. This occurs because of the convective cooling at the hole inlet, which improves with increase in the hole wall velocity, while the temperature gradient increases with increase in the hole wall temperature. The values of the Nusselt number for both jet velocities are almost the same, except at the hole inlet and the exit; the jet velocity of 100 m/s results in relatively higher Nusselt than that of 50 m/s.

Figure 9 shows the skin friction along the hole wall for two jet and six hole wall velocities. It should be noted that the dimensionless distance 0 represents the hole inlet while 2 corresponds to the hole exit. The skin friction is high at the hole inlet and it reduces sharply with increase

DOI: 10.1002/fld

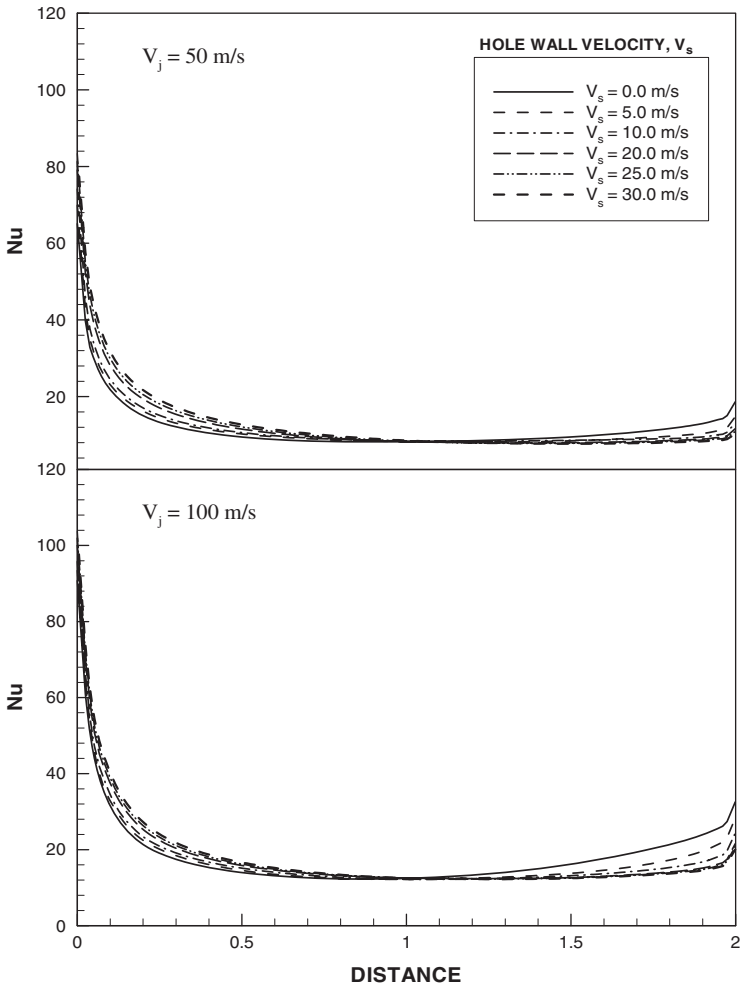

Figure 8. The Nusselt number along the hole wall for two mean jet velocities at nozzle exit. The distance is normalized by dividing the nozzle exit diameter (D). Taper angle is 45°.

in the distance along the hole wall. However, as the distance increases further toward the hole exit, the skin friction increases sharply, particularly in the vicinity of the hole exit. The attainment of the high skin friction is associated with the high rate of fluid strain developed in the inlet and the exit regions of the hole. Moreover, convective acceleration toward the hole exit, because of hole convergence, contributes significantly to the enhancement of the rate of fluid strain in this region. The effect of the hole wall velocity at hole inlet and exit regions is visible. In this case, increasing the hole wall velocity increases the skin friction in the hole inlet region. This is because of the radial flow due to streamline curvature and the wall velocity, which enhance the rate of fluid strain in this region. When comparing the jet velocities, the skin friction attains low values with increasing jet velocity, particularly in the inlet region of the hole.

DOI: 10.1002/fld

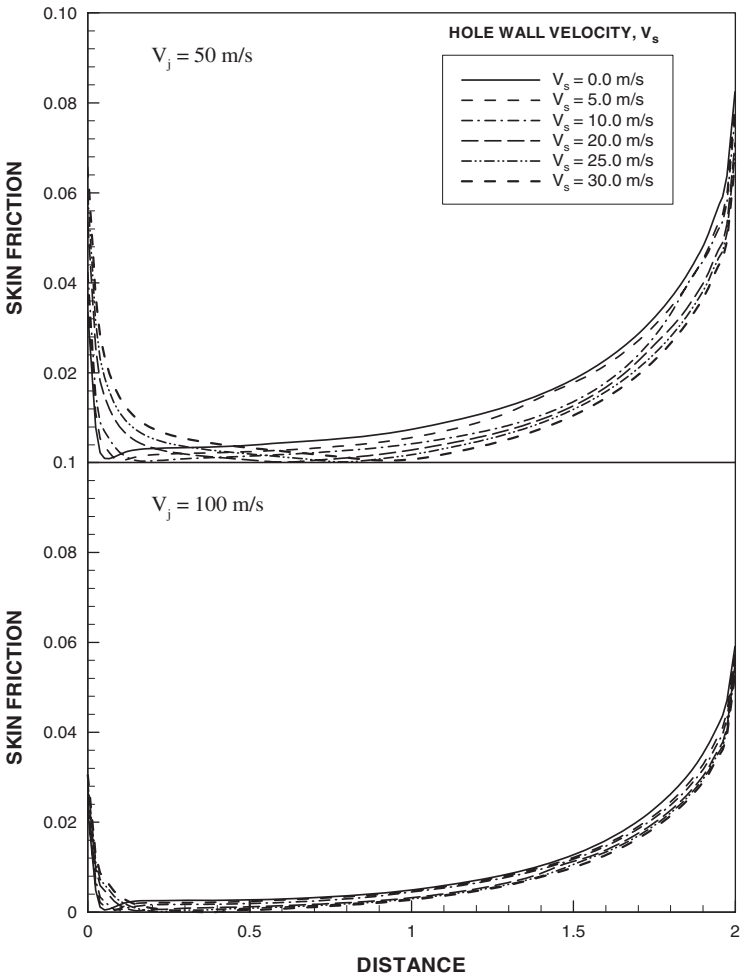

Figure 9. The skin friction along the hole wall for two mean jet velocities at nozzle exit. The distance is normalized by dividing the nozzle exit diameter (D). Taper angle is 45°.

Figure 10 shows the mass flow rate ratio with the hole wall velocity for two jet velocities. The mass flow rate ratio represents the ratio of the mass flow rate passing through the hole and mass flow rate emerging from the nozzle. The mass flow rate passing through the hole is almost only 10% of the impinging flow. This is because of the blockage effect of the hole. In this case, streamline curvature of the flow prior to entering to the hole, the hole tapering, and the thermodynamic pressure in the vicinity of the hole wall, due to high temperature, are responsible for the blockage effect. The effect of jet pressure on the mass flow rate ratio is not considerable. This suggests that the hole tapering plays a major role on the blockage effect as compared with the streamline curvature and the thermodynamic pressure. Moreover, the effect of the hole wall velocity on the mass flow rate ratio is not significant. Consequently, thinning of the boundary layer in the near hole wall region does not contribute significantly to the mass flow passing through the hole.

DOI: 10.1002/fld

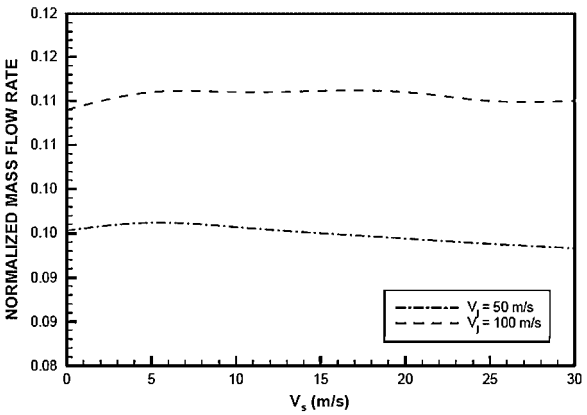

Figure 10. Mass flow ratio with hole wall velocity for two jet velocities. Mass flow ratio is determined from the ratio of mass flow rate emanating from nozzle to mass flow rate passing through the tapered hole.

5. CONCLUSION

Jet impingement onto a tapered hole with elevated wall temperature is investigated in relation to laser processing. The flow field, heat transfer characteristics, and the skin friction are predicted numerically. Since the flow field is turbulent, the Reynolds Stress Turbulence (RSM) is accommodated to account for the turbulence. The hole wall is set to move with the velocity of a molten surface, which is less than jet velocity according to a previous study. Therefore, the effect of the hole wall velocity on the Nusselt number and the skin friction is investigated. It is found that the flow field at the hole inlet is influenced by the streamline curvature of the impinging jet. In this case, radial momentum enables fluid to flow toward the hole wall region. This is more pronounced in the region close to the edge of the flow. The flow field in the entrance region of the hole is influenced by the blockage effect of the hole. The influence of the hole wall velocity on the Nusselt number is not significant, except for a small effect observed at the hole inlet and the exit regions. In this case, the Nusselt number increases slightly with increase in the hole wall velocity at the entry region of the hole while it is reduced by increasing the hole velocity at the exit region of the hole. Increasing the jet velocity increases the Nusselt number along the hole wall. The skin friction attains high values at the hole inlet and the exit. Increasing jet velocity enhances the skin friction at the hole inlet region while it is opposite at the hole exit region. Increasing jet velocity lowers the value of the skin friction. The mass flow rate ratio indicates that almost 10% of the jet mass flow rate enters into the hole and the effect of the hole tapering plays an important role for the attainment of the low mass flow rate ratio.

APPENDIX: NOMENCLATURE

H enthalpy
K thermal conductivity
k turbulent kinetic energy

DOI: 10.1002/fld

p	pressure
P	rate of production
R_{ij}	Reynolds stress
Re	Reynolds no.
r	distance in the radial direction
t	time
T	temperature
u^*	friction velocity
U	arbitrary velocity
V	axial velocity component
$\forall$	volume
x	distance in the axial direction

Greek letters

α	thermal diffusivity
Γ	arbitrary diffusion coefficient
ε	energy dissipation
λ	turbulence intensity
Λ	energy transport by diffusion
μ	dynamic viscosity
v	kinematic viscosity
ρ	density (function of temperature and pressure for gas)
σ	variable Prandtl no.
θ	nozzle cone angle
Φ	viscous dissipation
Π	energy transport due to pressure excluding strain interactions
Π^{w}	energy transport due to wall reflection
ϕ	arbitrary variable

Subscripts

amb	ambient
i, j	arbitrary direction
jet	gas jet at inlet
l	laminar
max	maximum
p	a typical node in the computational grid
t	turbulent
v	viscous sub-layer
w	wall

ACKNOWLEDGEMENTS

The authors acknowledge the support of King Fahd University of Petroleum and Minerals, Dhahran, Saudi Arabia.

DOI: 10.1002/fld

REFERENCES

1. Brignoni LA, Garimella SV. Effects of nozzle-inlet chamfering on pressure drop and heat transfer in confined air jet impingement. *International Journal of Heat and Mass Transfer* 2000; **43**:1133–1139.
2. Jungho L, Lee SJ. The effect of nozzle aspect ratio on stagnation region heat transfer characteristics of elliptic impinging jet. *International Journal of Heat and Mass Transfer* 2000; **43**:555–575.
3. Souris N, Liakos H, Founti M. Impinging jet cooling on concave surfaces. *AIChE Journal* 2004; **50**(8): 1672–1683.
4. Huang L, El-Genk MS. Heat transfer of an impinging jet on a flat surface. *International Journal of Heat and Mass Transfer* 1994; **27**(13):1915–1923.
5. Yang G, Choi M, Lee JS. An experimental study of slot jet impingement cooling on concave surface: effects of nozzle configuration and curvature. *International Journal of Heat and Mass Transfer* 1999; **42**(12):2199–2209.
6. Lytle D, Webb BW. Air jet impingement heat transfer at low nozzle-plate spacings, Heat Mass Transfer94. *Proceedings of the First ISHMT-ASME Heat Mass Transfer Conference*, Bombay, India, 1994; 271–276.
7. Cziesla T, Biswas G, Chattopadhyay H, Mitra NK. Large-eddy simulation of flow and heat transfer in an impinging slot jet. *International Journal of Heat and Fluid Flow* 2001; **22**(5):500–508.
8. Lee D, Greif R, Lee SJ, Lee JH. Heat transfer from a flat plate to a fully developed axisymmteric impinging jet. *Journal of Heat Transfer* 1995; **117**:772–776.
9. Colucci DW, Viskanta R. Effect of nozzle geometry on local convective heat transfer to a confined impinging air jet. *Experimental Thermal and Fluid Science* 1996; **13**(1):71–80.
10. Amano RS, Brandt H. Numerical study of turbulent axisymmetric jets impinging on a flat plate and flowing into an axisymmteric cavity. *Journal of Fluids Engineering* 1984; **106**:410–417.
11. Shuja SZ, Yilbas BS, Budair MO. Influence of conical and annular nozzle geometric configurations on flow and heat transfer characteristics due to flow impingement onto a flat plate. *Numerical Heat Transfer*, *Part A*, vol. 48. 2005; 917–939.
12. Shuja SZ, Yilbas BS, Budair MO. Jet impingement on cylindrical cavity: conical nozzle considerations. *Journal of Fluids and Structures* 2007; **23**:1106–1118.
13. Yilbas BS, Shuja SZ, Budair MO. Jet impingement onto a hole with constant wall temperature. *Numerical Heat Transfer* 2003; **43**:843–865.
14. Yilbas BS, Abdul Aleem BJ. Dross formation during laser cutting process. *Journal of Physics Part D*: *Applied Physics* 2006; **39**:1451–1461.
15. Launder BE. Second-moment closure and its use in modelling turbulent industrial flows. *International Journal for Numerical Methods in Fluids* 1989; **9**:963–985.
16. Hogg S, Leschziner MA. Second-moment-closure calculation of strongly swirling confined flow with large density gradients. *International Journal of Heat and Fluid Flow* 1989; **10**:16–271.
17. Elkaim D, Reggio M, Camarero R. Simulating two-dimensional turbulent flow by using the k–ε model and the vorticity-stream function formulation. *International Journal for Numerical Methods in Fluids* 1992; **14**:961–980.
18. Patankar SV. *Numerical Heat Transfer*. McGraw-Hill: New York, 1980.
19. Cooper D, Jackson DC, Launder BE, Liao GX. Impinging jet studies for turbulence model assessment—I: flow-field experiments. *International Journal of Heat and Mass Transfer* 1993; **36**:2675–2684.

DOI: 10.1002/fld